Improved 2D vector field estimation using probabilistic weights

Archontis Giannakidis[1] and Maria Petrou[2,*]

[1]*Faculty of Engineering Physical Sciences, University of Surrey, Guildford GU2 7XH, UK*
[2]*Department of Electrical and Electronic Engineering, Imperial College, London SW7 2AZ, UK*
*Corresponding author: maria.petrou@imperial.ac.uk

We consider the application of tomography to the reconstruction of two-dimensional vector fields. The most practical sensor configuration in such problems is the regular positioning along the boundary of the reconstruction domain. However, such a configuration does not result in uniform distribution in the Radon parameter space, which is a necessary requirement to achieve accurate reconstruction results. On the other hand, sampling the projection space uniformly imposes serious constraints on space or time. In this paper, we propose to place the sensors regularly along the boundary of the reconstruction domain and employ probabilistic weights with the purpose of compensating for the lack of uniformity in the distribution of projection space parameters. Simulation results demonstrate that, when the proposed probabilistic weights are employed, an average 27% decrease in the reconstruction error may be achieved, over the case that projection measurements are not weighed (e.g., in one case the error reduces from 3.7% to 2.6%). When compared with the case where actual uniform sampling of the projection space is employed, the proposed method achieves a 90 times reduction in the number of the required sensors or 180 times reduction in the total scanning time, with only 7% increase in the error with which the vector field is estimated.   © 2011 Optical Society of America

OCIS codes: 110.6960, 110.6955, 110.3010, 100.6950, 100.3190.

1. INTRODUCTION

Vectors of flow velocity, stress, electric field, magnetic field, and gradient of the refractive index may be used to characterize the internal structure of a system. The imaging technique that allows one to elicit these vector quantities without physically probing the interior of the examined system is called vector field tomography. To achieve reconstruction, vector field tomography relies on projection measurements of the inner product of the investigated vector field with a fixed vector.

Vector field tomography may be used in a wide variety of disciplines. Some of the application areas that have been considered include medicine [1,2], plasma physics [3], oceanography [4–6], fluid dynamics [7–14], optics [12,15–18], photoelasticity [19,20], nuclear fusion [21], and studies of heating devices [22].

When we try to investigate planar vector fields in bounded domains, two versions of the vectorial Radon transform are relevant, depending on the type of measurements obtained:

$$J_1 = \int_L \bar{\mathbf{f}}(x,y) \cdot \hat{\mathbf{s}} \mathrm{d}s = \int_L f_\parallel \mathrm{d}s, \qquad (1)$$

$$J_2 = \int_L \bar{\mathbf{f}}(x,y) \cdot \hat{\rho} \mathrm{d}s = \int_L f_\perp \mathrm{d}s. \qquad (2)$$

Here, $\bar{\mathbf{f}}(x,y)$ is the planar vector field under investigation, $\hat{\mathbf{s}}$ is the unit vector along the integration (measurement) line L, ds is an element of path length along this line, the middot is the symbol for the dot product of two vectors, $f_\parallel$ is the component of $\bar{\mathbf{f}}(x,y)$ along L, $\hat{\rho}$ is the unit vector perpendicular to the line of integration L, and $f_\perp$ is the component of $\bar{\mathbf{f}}(x,y)$ transverse to L. From Eq. (1), we may deduce that only the component of $\bar{\mathbf{f}}(x,y)$ along the line L is observed in this type of measurement (longitudinal measurements), while, in the second case, J_2 is used to model tomographic measurements that collect information from the component of the investigated vector field perpendicular to the measurement line (transversal measurements).

The problem of reconstructing the two-dimensional (2D) vector field either from longitudinal or transversal measurements in the continuous domain has been shown to be underdetermined [11,12,19,23]. In particular, it was found that only one component of the vector field could be recovered from tomographic measurements. The recovered component was either the curl-free (irrotational) part or the divergence-free (solenoidal) part, depending on the physical principle of the measurements of the considered application. An algebraic reconstruction method of this type, where the authors considered the problem of only reconstructing the solenoidal component from the tomographic data, was developed in [24]. To recover the vector field fully, one should collect data using both types of measurements [12]. Unfortunately, there are only very few specialized applications (mainly in Schlieren tomography), where it is physically realizable to have both types of measurement available. Another solution was proposed by Norton [11], who suggested that one may have a full reconstruction based only on longitudinal measurements, as long as, apart from the longitudinal measurements, supplementary information about the investigated vector field, especially boundary conditions or *a priori* information about its source distribution, is available as well. A study, where the developed algebraic methodology was about reconstructing a vector field based on longitudinal measurements and *a priori* information about the source distribution of the vector field

to be imaged, was presented in [25]. Another similar example of using, apart from the projection measurements, supplementary information about the examined vector field lies in meteorology [26]. The supplementary information that the authors of [26] employed about the examined wind velocity field was in the form of angle measurements. Rouseff and Winters showed in [27] that a 2D vector field reconstruction based on boundary data is possible for scattering geometries. However, the model they used for the available measurements was a scattering model rather than the integral-geometry transformations of Eqs. (1) and (2) that have been traditionally used in vector field tomography and are based on transmission.

It has recently been demonstrated [28], however, that in the digital domain one may obtain a pretty good estimate of a 2D vector field, using only a finite number of projection measurements, as long as the field is band limited and the sampling does not violate the Nyquist criterion. Under these assumptions, it was shown that one may achieve an estimate of both components of a 2D vector field at a finite number of sampling points of its domain, based only on boundary integral information, by simply exploiting the redundancy in the projection data and the inaccuracies introduced by the digitization process as a form of implicit regularization. The regularization lies in the fact that digitization error prevents the system matrix from being rank deficient, while by using many line orientations passing through every sampling point, and then viewing the related recordings as weighted sums of the local vector field's Cartesian components, one can estimate reasonably well the unknown vector field by solving a least-squares estimation problem.

The method proposed in [28] is a direct algebraic reconstruction technique. This technique treats the discretized available measurements as bounded linear functionals on the space of two-integrable functions in the reconstruction region. Hence, the 2D vector field estimation problem is cast as the solution of a system of linear equations, where the unknowns of the system are the Cartesian components of the examined vector field in specific sampling points, finite in number and arranged in a grid. However, there is a duality between this matrix formalism and the vectorial Radon transform scheme. Hence, solving the above described system of linear equations is equivalent to inverting the vectorial Radon transform.

According to the theory of the Radon transform [29], a necessary requirement to produce reconstruction results with the accuracy desired in medical imaging, when using discrete approximations, is to sample uniformly the Radon domain parameter space, defined by the length of the normal to a scanning line, ρ, and the angle this normal forms with the positive x semiaxis, θ (see Fig. 1). The technique, which was proposed in [28], assumed that the measurements were collected by sensors that followed uniform distribution in the space of the Cartesian intersection coordinates with the boundary of the reconstruction domain. Such a sensor placement might be the most practical, however, it does not result in scanning lines that follow uniform distribution in the (ρ, θ) projection space. On the other hand, sampling the Radon parameter domain uniformly has the following major drawbacks.

i.   It dictates a prohibitively large number of sensors.

ii.   It results in impractical sensor positioning. In particular, the uniform sampling of the (ρ, θ) space dictates that the sensors that have to be placed at the ends of a scanning line may be impractically close to the sensors of another scanning line.

In the case where the sensors may be mounted on a common rotating frame, the problems described in (i) and (ii) regarding the uniform sampling of the Radon parameter domain are no longer present. However, in this case, each scan of the domain corresponds to only one value of the angular parameter. Hence, in order to cover all angular orientations, the scanning process needs to be repeated many times. This leads to prohibitively large total scanning times and it cannot be applied to the medical field, where the scanning time is crucial.

In this paper, we compensate for the lack of uniform sampling in the (ρ, θ) projection space by employing weights. These weights are obtained by calculating the probability density function of (ρ, θ) when the sensors are placed uniformly along the boundary of the reconstruction domain. Hence, the proposed modification to the direct algebraic reconstruction technique presented in [28] accounts for the nonuniform density of the projection space by inversely weighing every equation (measurement) according to the local (ρ, θ) density of the scanning line associated with this equation, and, also, multiplying with the (uniform) probability mass that the pair (ρ, θ) should have. It must be noted that, due to the fact that the calculation of the proposed weights is based on the known and predetermined sensor arrangement, this calculation can be performed in advance (offline).

This paper is organized as follows. In Section 2, we formulate the problem, set up our notation, and present a brief summary of the initial direct algebraic estimation method presented in [28]. In Section 3, we work out the weights that should be employed in the estimation process. In Section 4, we present an example of static electric field estimation to demonstrate the effect of the employment of the proposed probabilistic weights on the quality of the estimation. We conclude in Section 5.

2. INITIAL ESTIMATION TECHNIQUE

In this section, we review the direct algebraic estimation methodology that was presented in [28]. The whole treatment is performed in the digital domain. Let us assume that we have the digitized square 2D domain that is shown in Fig. 1, within which we want to estimate vector field $\bar{\mathbf{f}}(x, y) = f_x(x, y)\hat{\mathbf{x}} + f_y(x, y)\hat{\mathbf{y}}$. The length of each side of the square domain is taken to be equal to $2U$ and the origin of the axes of the coordinate system is chosen to be at the center of the domain. The square domain is sampled with a regular grid of samples and the distance between any two adjacent samples along either of the axes is equal to P. For simplicity, we assume that P is such that $K \equiv 2U/P$ is an integer. The goal is to estimate vector field $\bar{\mathbf{f}}(x, y)$ at the sampling points of the domain.

Regarding the data acquisition, we assume that ideal point sensors, which integrate only the component of the field projected on the line, reside on predetermined and regularly placed positions of the whole border of the 2D square domain, at P distance apart (see Fig. 1). Hence, there are $\frac{2U}{P}$ ideal point sensors on each side of the boundary of the domain.
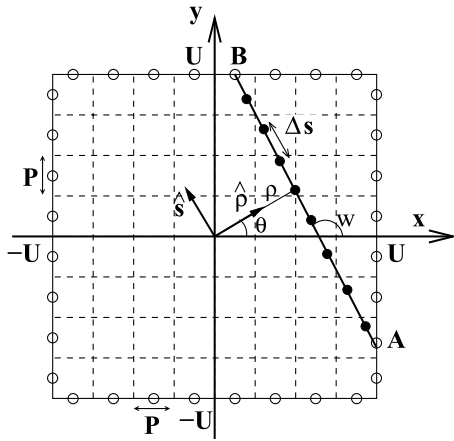
Fig. 1.   Digitized reconstruction region is a square of size $2U$. The size of the pixels, with which we sample the 2D space, is $P \times P$. Open circles represent the known and predetermined sensor positions from which we obtain the line-integral data. These positions are the middle points of the boundary edges of all boundary pixels. A scanning line segment AB is sampled with sampling step Δs. The angle between the line segment and the positive direction of the x axis is w. Also shown are the two parameters ρ and θ used to define the scanning line (projection space coordinates) and the unit vectors $\hat{s}$ and $\hat{\rho}$, which are parallel and perpendicular, respectively, to line segment AB.

The employed sensor arrangement yields a set of scanning lines. Let us consider a scanning line AB that belongs to this set and connects two boundary sensors located at points A and B, chosen arbitrarily (see Fig. 1). Then, scanning line AB yields a line-integral measurement. Since we assumed that a pair of sensors measures only the integral of the component of the investigated vector field along the scanning line, the integral transform that models this measurement is given by

$$J_i = \int_{AB} \bar{\mathbf{f}}(x,y) \cdot \hat{\mathbf{s}}_i \mathrm{d}s. \tag{3}$$

Here, $\hat{\mathbf{s}}_i = \cos w \hat{\mathbf{x}} + \sin w \hat{\mathbf{y}}$ is the unit vector along the integration line AB, where w is the angle between the scanning line and the positive direction of the x axis (see Fig. 1). In addition, $\mathrm{d}s$ is an element of path length along this line.

Next, Eq. (3) is written in digital form and the samples of the field along each line are expressed in terms of the components of the 2D vector field we wish to estimate using nearest neighbor interpolation:

$$J_i = \sum_l \bar{\mathbf{f}}_l \cdot \overline{\Delta \mathbf{s}}_i, \tag{4}$$

where $\bar{\mathbf{f}}_l = (f_{xl}, f_{yl})$ are the unknown vector field values at sampling points l and $\overline{\Delta \mathbf{s}}_i = \Delta s \hat{\mathbf{s}}_i$, with Δs being the sampling step of the line.

In order to obtain the system of linear equations, the solution of which will give the components of the examined vector field $\bar{\mathbf{f}}(x, y)$ at all sampling points of the 2D domain, the procedure described above is repeated for all possible pairs of boundary point sensors that yield integral measurements along scanning lines, apart from pairs of sensors that reside on the same side of the boundary of the square and are not useful. Hence, the number of the available Eqs. (4) depends on the selection of the data acquisition geometry. In general, this selection leads to an overdetermined system of linear equations, in accordance with our intention to take advantage of the redundancy in the line-integral data, as a form of employing regularization to deal with the ill-posed nature of the 2D vector field reconstruction problem. Therefore, the least-square error solution is worked out.

In Eqs. (4), J_i is the measurement obtained by integrating along scanning line AB. This line is defined, in terms of projection space parameters ρ and θ, by using the Hessian normal form

$$\rho = x \cos \theta + y \sin \theta, \tag{5}$$

where parameters ρ and θ have been defined in Fig. 1 and, also, $\rho \geq 0$ and $-\pi < \theta \leq \pi$. Hence, there is a pair of (ρ, θ) parameter values associated with each line-integral measurement. However, it is important to note that, by placing the sensors uniformly distributed in the space of the Cartesian intersection coordinates with the boundary of the domain, as proposed in [28], the distribution of the (ρ, θ) parameters of the resulting scanning lines is not uniform. According to the theory of the Radon transform [29], failure to achieve uniformity in the (ρ, θ) parameters results in loss of accuracy in the reconstruction results.

In this paper, we propose to compensate for the lack of uniformity in the (ρ, θ) parameters of the scanning lines by employing weights. In particular, to account for the nonuniform (ρ, θ) density of the set of scanning lines, every equation is inversely weighed according to the local (ρ, θ) density of the scanning line associated with this equation, and multiplied with the (uniform) probability that the pair (ρ, θ) should have. In the next section, we work out the weights that should be employed in the estimation process.

3. WEIGHTED ESTIMATION METHODOLOGY

In this paper, we propose to modify the direct algebraic estimation technique, which was introduced in [28] and reviewed in Section 2, by employing probabilistic weights. These weights should be multiplied with the equations of the system, obtained following the analysis in [28], so as to account for the nonuniformity in the (ρ, θ) space. Note that, although each equation of the linear system is supposed to equal 0, and therefore multiplication with a constant should not make any difference to the equation, the constant used weighs the residual with which each equation is satisfied and thus affects the least-square error solution obtained. It should also be stressed that, due to digitization errors, no equation of the linear system is expected to be satisfied exactly, even if we do not assume any other source of noise, i.e., in general, there will always be a residual error with which each equation is satisfied.

Before we calculate the proposed weights, we first attempt to answer the following question: given the employed scanning geometry of Fig. 1, where the sensors are uniformly distributed along the boundary of the domain, what is the distribution of the (ρ, θ) parameters of the resulting scanning lines?

Let us call (x_1, y_1) and (x_2, y_2) the end points of an arbitrary scanning line segment that goes through the reconstruction region of Fig. 1. Our first task is to express parameters (ρ, θ) in terms of the intersection parameters (sensor Cartesian

coordinates). We then go on to work out the distribution of parameters (ρ, θ).

Intersection parameters x_1, y_1, x_2, and y_2 are not independent, as they are the coordinates of points constrained to be on the domain border. For this reason, we have the following possibilities for a scanning line.

1. A scanning line where the two sensors lie on the domain borders $y = -U$ and $x = U$ (Fig. 2). The coordinates of the two sensors are $(x_1, -U)$ and (U, y_2). Both sensors lie on the scanning line (ρ, θ). Hence, Eq. (5) yields

$$\rho = x_1 \cos\theta - U \sin\theta, \tag{6}$$

$$\rho = U \cos\theta + y_2 \sin\theta. \tag{7}$$

In order to determine the joint probability density function of parameters ρ and θ, the Cartesian sensor coordinates x_1 and y_2 are treated as random variables. By making the assumption that there are infinitely many sensors, these sensor coordinates may take any value in the range $(-U, U)$ with the same probability. We make this assumption in order to reduce the computational complexity. Hence, x_1 and y_2 are uniformly distributed random variables with corresponding density functions

$$f_{x_1}(x_1) = \frac{1}{2U}[H(x_1 + U) - H(x_1 - U)], \tag{8}$$

$$f_{y_2}(y_2) = \frac{1}{2U}[H(y_2 + U) - H(y_2 - U)]. \tag{9}$$

In the above formulas, $H()$ is the Heaviside step function, the value of which is 0 for a negative argument and 1 for a positive argument.

Since the value of coordinate x_1 is independent of the value of coordinate y_2, these two variables are statistically independent. Hence, the joint probability density function of x_1 and y_2, $f_{x_1 y_2}(x_1, y_2)$, is given by

$$
\begin{aligned}
f_{x_1 y_2}(x_1, y_2) &= f_{x_1}(x_1) f_{y_2}(y_2) \\
&= \frac{1}{4U^2}[H(x_1 + U) - H(x_1 - U)][H(y_2 + U) \\
&\quad - H(y_2 - U)].
\end{aligned}
\tag{10}
$$

From Eqs. (6) and (7) it follows that

$$\theta = \arctan\frac{x_1 - U}{y_2 + U}, \tag{11}$$
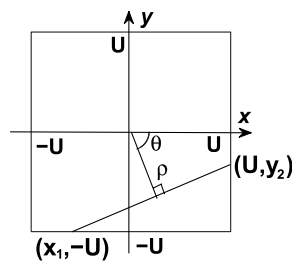

Fig. 2.   First case of scanning lines.

$$\rho = x_1 \cos\left(\arctan\frac{x_1 - U}{y_2 + U}\right) - U \sin\left(\arctan\frac{x_1 - U}{y_2 + U}\right). \tag{12}$$

In this paper, we restrict the inverse function arctan to take only its principal values, i.e., values in the range $(-\frac{\pi}{2}, \frac{\pi}{2})$.

The following fundamental theorem is valid [30]: if ρ and θ are two functions of two random variables x_1 and y_2

$$\rho = h(x_1, y_2), \tag{13}$$

$$\theta = g(x_1, y_2), \tag{14}$$

we may express the joint probability density function of ρ and θ, $f_{\rho\theta}(\rho, \theta)$, in terms of the joint probability density function of x_1 and y_2, $f_{x_1 y_2}(x_1, y_2)$, as

$$f_{\rho\theta}(\rho, \theta) = \frac{f_{x_1 y_2}(x_{1_a}, y_{2_a})}{|J(x_{1_a}, y_{2_a})|} + \cdots + \frac{f_{x_1 y_2}(x_{1_k}, y_{2_k})}{|J(x_{1_k}, y_{2_k})|}, \tag{15}$$

where

$$J(x_1, y_2) = \begin{vmatrix} \frac{\partial\rho}{\partial x_1} & \frac{\partial\rho}{\partial y_2} \\ \frac{\partial\theta}{\partial x_1} & \frac{\partial\theta}{\partial y_2} \end{vmatrix} = \begin{vmatrix} \frac{\partial x_1}{\partial\rho} & \frac{\partial x_1}{\partial\theta} \\ \frac{\partial y_2}{\partial\rho} & \frac{\partial y_2}{\partial\theta} \end{vmatrix}^{-1} \tag{16}$$

is the Jacobian determinant of the transformation of Eqs. (13) and (14), and $(x_{1_a}, y_{2_a}), \ldots, (x_{1_k}, y_{2_k})$ are the k real roots of the system of the same equations.

For the considered set of scanning lines, we have $\rho > 0$ and $\theta \in (-\frac{\pi}{2}, 0)$. Hence, the system of Eqs. (11) and (12) has a single solution:

$$(x_{1_a}, y_{2_a}) = \left(\frac{\rho}{\cos\theta} + U\tan\theta, \frac{\rho}{\sin\theta} - U\cot\theta\right). \tag{17}$$

This solution is obtained by solving Eqs. (6) and (7) with respect to x_1 and y_2, and, also, taking into account that $\cos\theta \neq 0$ and $\sin\theta \neq 0$ for the examined set of scanning lines. Considering Eq. (17), we obtain from Eq. (16):

$$
\begin{aligned}
J(x_{1_a}, y_{2_a}) &= \begin{vmatrix} \frac{1}{\cos\theta} & \frac{\rho\sin\theta}{\cos^2\theta} + \frac{U}{\cos^2\theta} \\ \frac{1}{\sin\theta} & \frac{-\rho\cos\theta}{\sin^2\theta} + \frac{U}{\sin^2\theta} \end{vmatrix}^{-1} \\
&= \left[\frac{U - \rho\cos\theta}{\cos\theta\sin^2\theta} - \frac{U + \rho\sin\theta}{\sin\theta\cos^2\theta}\right]^{-1} \\
&= \left[\frac{U(\cos\theta - \sin\theta) - \rho}{\cos^2\theta\sin^2\theta}\right]^{-1}. \tag{18}
\end{aligned}
$$

For the examined scanning lines (ρ, θ), we have $U(\cos\theta - \sin\theta) - \rho \neq 0$. Hence, Eq. (18) yields

$$J(x_{1_a}, y_{2_a}) = \frac{\cos^2\theta\sin^2\theta}{U(\cos\theta - \sin\theta) - \rho}. \tag{19}$$

Taking into account Eqs. (17) and (19), we conclude from Eq. (15) that

$$
\begin{aligned}
f_{\rho\theta}^1(\rho, \theta) &= \left|\frac{U(\cos\theta - \sin\theta) - \rho}{\cos^2\theta\sin^2\theta}\right| \\
&\quad \times f_{x_1 y_2}\left(\frac{\rho}{\cos\theta} + U\tan\theta, \frac{\rho}{\sin\theta} - U\cot\theta\right). \tag{20}
\end{aligned}
$$

Finally, by substituting Eq. (10) into Eq. (20), we obtain that the joint probability density function of ρ and θ, for this set of scanning lines, is given by

$$
\begin{aligned}
f^1_{\rho\theta}(\rho,\theta) = \frac{\left|\frac{U(\cos\theta-\sin\theta)-\rho}{\cos^2\theta\sin^2\theta}\right|}{4U^2} & \left[H\left(\frac{\rho}{\cos\theta}+U\tan\theta+U\right)\right.\\
& \left.-H\left(\frac{\rho}{\cos\theta}+U\tan\theta-U\right)\right]\\
& \times\left[H\left(\frac{\rho}{\sin\theta}-U\cot\theta+U\right)\right.\\
& \left.-H\left(\frac{\rho}{\sin\theta}-U\cot\theta-U\right)\right].
\end{aligned}
\tag{21}
$$

2.   A scanning line where the two sensors lie on the domain borders $y=-U$ and $x=-U$ (Fig. 3). The result in this case may be obtained straightforwardly from Eq. (20) by exploiting the symmetries of the problem and setting $\theta\to\theta-\pi/2$, $x_1\to y_2$, and $y_2\to -x_1$. The result is

$$
\begin{aligned}
f^2_{\rho\theta}(\rho,\theta) = \frac{\left|\frac{U(\cos\theta+\sin\theta)+\rho}{\cos^2\theta\sin^2\theta}\right|}{4U^2} & \left[H\left(\frac{\rho}{\cos\theta}+U\tan\theta+U\right)\right.\\
& \left.-H\left(\frac{\rho}{\cos\theta}+U\tan\theta-U\right)\right]\\
& \times\left[H\left(\frac{\rho}{\sin\theta}+U\cot\theta+U\right)\right.\\
& \left.-H\left(\frac{\rho}{\sin\theta}+U\cot\theta-U\right)\right].
\end{aligned}
\tag{22}
$$

3.   A scanning line where the two sensors lie on the domain borders $x=U$ and $y=U$ (Fig. 4). The result for this case may be obtained from Eq. (20) by setting $\theta\to\theta+\pi/2$, $x_1\to -y_2$, and $y_2\to x_1$:

$$
\begin{aligned}
f^3_{\rho\theta}(\rho,\theta) = \frac{\left|\frac{U(\cos\theta+\sin\theta)-\rho}{\cos^2\theta\sin^2\theta}\right|}{4U^2} & \left[H\left(\frac{\rho}{\cos\theta}-U\tan\theta+U\right)\right.\\
& \left.-H\left(\frac{\rho}{\cos\theta}-U\tan\theta-U\right)\right]\\
& \times\left[H\left(\frac{\rho}{\sin\theta}-U\cot\theta+U\right)\right.\\
& \left.-H\left(\frac{\rho}{\sin\theta}-U\cot\theta-U\right)\right].
\end{aligned}
\tag{23}
$$

4.   A scanning line where the two sensors lie on the domain borders $y=U$ and $x=-U$ (Fig. 5). The result for this case
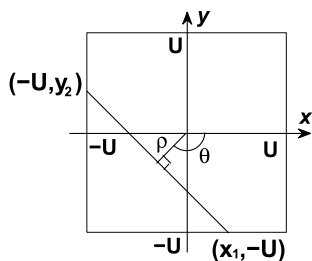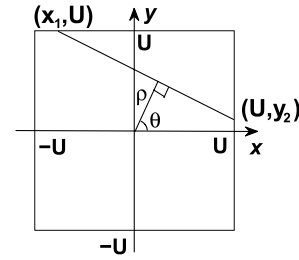

Fig. 3.   Second case of scanning lines.

Fig. 4.   Third case of scanning lines.

may be obtained from Eq. (20) by setting $\theta\to\theta+\pi$, $x_1\to -x_1$, and $y_2\to y_2$:

$$
\begin{aligned}
f^4_{\rho\theta}(\rho,\theta) = \frac{\left|\frac{U(\sin\theta-\cos\theta)-\rho}{\cos^2\theta\sin^2\theta}\right|}{4U^2} & \left[H\left(\frac{\rho}{\cos\theta}-U\tan\theta+U\right)\right.\\
& \left.-H\left(\frac{\rho}{\cos\theta}-U\tan\theta-U\right)\right]\\
& \times\left[H\left(\frac{\rho}{\sin\theta}+U\cot\theta+U\right)\right.\\
& \left.-H\left(\frac{\rho}{\sin\theta}+U\cot\theta-U\right)\right].
\end{aligned}
\tag{24}
$$

5.   A scanning line where the two sensors lie on the domain borders $y=-U$ and $y=U$ (Fig. 6). The coordinates of the two sensors are $(x_1,-U)$ and (x_2,U). Both sensors lie on the scanning line (ρ,θ). Hence, Eq. (5) yields

$$
\rho = x_1\cos\theta - U\sin\theta,
\tag{25}
$$

$$
\rho = x_2\cos\theta + U\sin\theta.
\tag{26}
$$

Sensor coordinates x_1 and x_2 are treated as uniformly distributed random variables in the range $(-U,U)$. Hence, the probability density function of x_1 is determined by Eq. (8), whereas the corresponding density function of random variable x_2 is given by

$$
f_{x_2}(x_2) = \frac{1}{2U}[H(x_2+U)-H(x_2-U)].
\tag{27}
$$

Their joint probability density function is

$$
\begin{aligned}
f_{x_1 x_2}(x_1,x_2) &= f_{x_1}(x_1)f_{x_2}(x_2)\\
&= \frac{1}{4U^2}[H(x_1+U)-H(x_1-U)][H(x_2+U)\\
&\quad -H(x_2-U)].
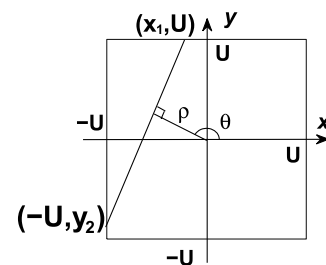\end{aligned}
\tag{28}
$$

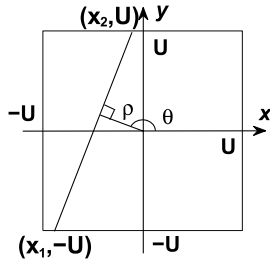

Fig. 5.   Fourth case of scanning lines.

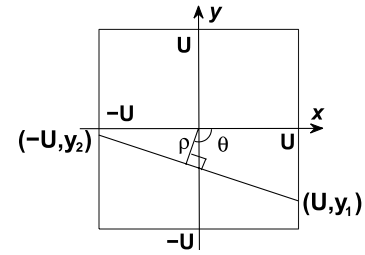Fig. 6.   Fifth case of scanning lines.

Fig. 7.   Sixth case of scanning lines.

For the examined set of scanning lines, we have $\rho \geq 0$ and $\theta \in (-\pi, -\frac{3\pi}{4}) \cup (-\frac{\pi}{4}, \frac{\pi}{4}) \cup (\frac{3\pi}{4}, \pi]$. The following cases have to be distinguished.

- When $\theta \in (-\pi, -\frac{3\pi}{4})$, it follows from Eqs. (25) and (26) that

$$\theta = \arctan\frac{x_1 - x_2}{2U} - \pi, \qquad (29)$$

$$\rho = x_1 \cos\left(\arctan\frac{x_1 - x_2}{2U} - \pi\right) - U \sin\left(\arctan\frac{x_1 - x_2}{2U} - \pi\right). \qquad (30)$$

- When $\theta \in (-\frac{\pi}{4}, \frac{\pi}{4})$, it follows from Eqs. (25) and (26) that
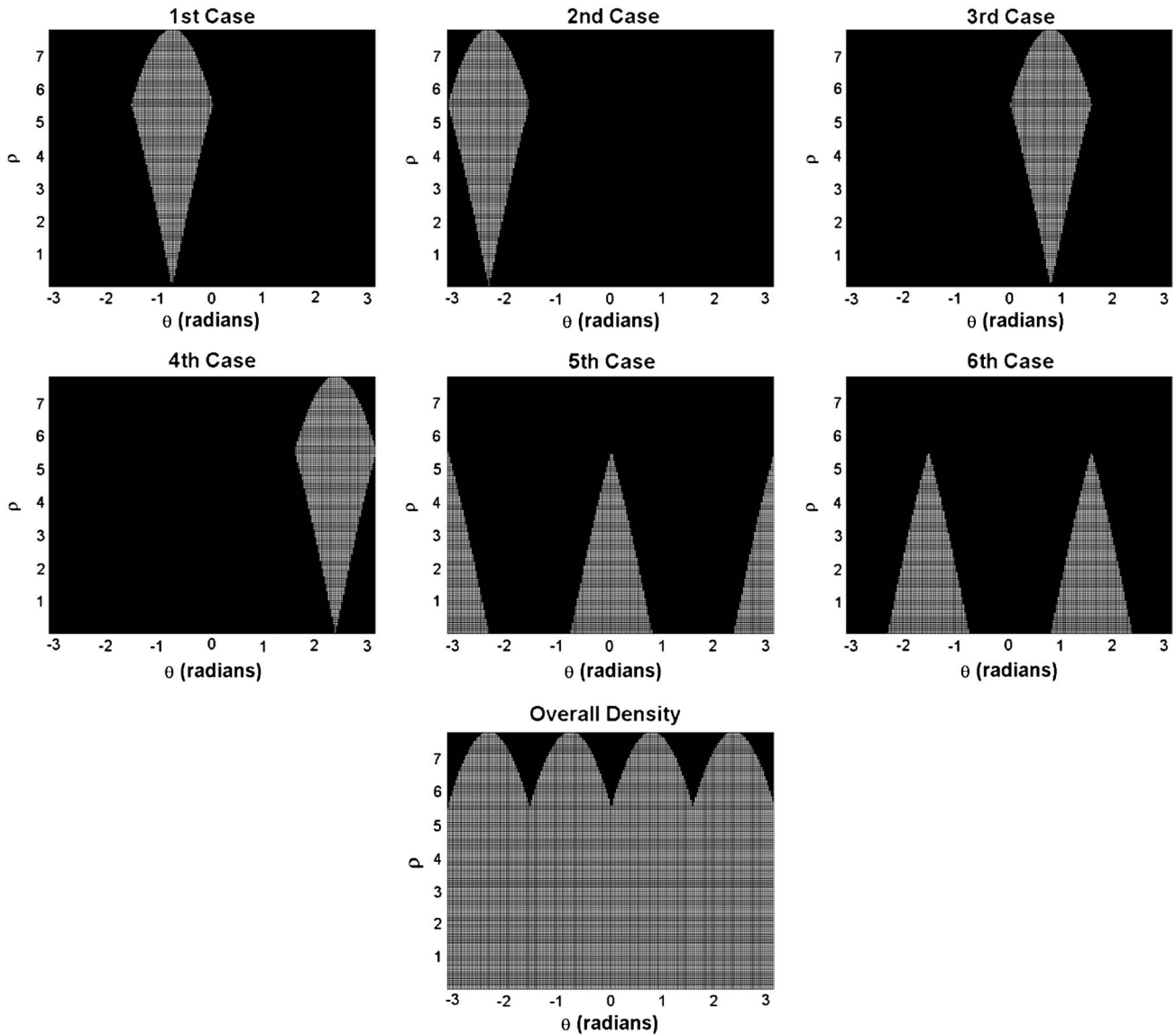
$$\theta = \arctan\frac{x_1 - x_2}{2U}, \qquad (31)$$

Fig. 8.   Areas that the six individual and the overall probability densities cover in the projection space.

$$\rho = x_1 \cos\left(\arctan\frac{x_1 - x_2}{2U}\right) - U\sin\left(\arctan\frac{x_1 - x_2}{2U}\right). \quad (32)$$

- When $\theta \in (\frac{3\pi}{4}, \pi]$, we obtain from Eqs. (25) and (26):

$$\theta = \arctan\frac{x_1 - x_2}{2U} + \pi, \quad (33)$$

$$\rho = x_1 \cos\left(\arctan\frac{x_1 - x_2}{2U} + \pi\right) - U\sin\left(\arctan\frac{x_1 - x_2}{2U} + \pi\right). \quad (34)$$

The three 2×2 systems of Eqs. (29)–(34) have all a single solution in the corresponding intervals of variable θ. This solution is given by the same formula for all three systems

$$(x_{1_a}, x_{2_a}) = \left(\frac{\rho}{\cos\theta} + U\tan\theta, \frac{\rho}{\cos\theta} - U\tan\theta\right) \quad (35)$$

and is obtained by solving Eqs. (25) and (26) with respect to x_1 and x_2, and, also, by taking into account that, for the examined set of scanning lines, $\cos\theta \neq 0$. As a result of this and the theorem expressed by Eqs. (13)–(16), the formula that determines the joint density $f^5_{\rho\theta}(\rho, \theta)$ will be common for all intervals of variable θ. Considering Eq. (35), the application of the theorem expressed by Eqs. (13)–(16), for random variables x_1 and x_2 and all three systems of Eqs. (29)–(34), yields

$$J(x_{1_a}, x_{2_a}) = \begin{vmatrix} \frac{\partial\rho}{\partial x_{1_a}} & \frac{\partial\rho}{\partial x_{2_a}} \\ \frac{\partial\theta}{\partial x_{1_a}} & \frac{\partial\theta}{\partial x_{2_a}} \end{vmatrix}$$
$$= \begin{vmatrix} \frac{\partial x_{1_a}}{\partial\rho} & \frac{\partial x_{1_a}}{\partial\theta} \\ \frac{\partial x_{2_a}}{\partial\rho} & \frac{\partial x_{2_a}}{\partial\theta} \end{vmatrix}^{-1} = \begin{vmatrix} \frac{1}{\cos\theta} & \frac{\rho\sin\theta}{\cos^2\theta} + \frac{U}{\cos^2\theta} \\ \frac{1}{\cos\theta} & \frac{\rho\sin\theta}{\cos^2\theta} - \frac{U}{\cos^2\theta} \end{vmatrix}^{-1} = -\frac{\cos^3\theta}{2U}. \quad (36)$$

Taking into account Eqs. (35) and (36), we conclude from the theorem that

$$f^5_{\rho\theta}(\rho, \theta) = \left|\frac{2U}{\cos^3\theta}\right| f_{x_1 x_2}\left(\frac{\rho}{\cos\theta} + U\tan\theta, \frac{\rho}{\cos\theta} - U\tan\theta\right). \quad (37)$$

Finally, by substituting Eq. (28) into Eq. (37), we obtain the joint probability density function of ρ and θ, for this set of scanning lines:

$$f^5_{\rho\theta}(\rho, \theta) = \frac{\left|\frac{2U}{\cos^3\theta}\right|}{4U^2}\left[H\left(\frac{\rho}{\cos\theta} + U\tan\theta + U\right)\right.$$
$$- H\left(\frac{\rho}{\cos\theta} + U\tan\theta - U\right)\right]$$
$$\times \left[H\left(\frac{\rho}{\cos\theta} - U\tan\theta + U\right)\right.$$
$$\left. - H\left(\frac{\rho}{\cos\theta} - U\tan\theta - U\right)\right]. \quad (38)$$

6.   A scanning line where the two sensors lie on the domain borders $x = U$ and $x = -U$ (Fig. 7). The coordinates of the

two sensors are (U, y_1) and $(-U, y_2)$. Both sensors lie on the scanning line (ρ, θ). Hence, Eq. (5) yields

$$\rho = U\cos\theta + y_1\sin\theta, \quad (39)$$

$$\rho = -U\cos\theta + y_2\sin\theta. \quad (40)$$

Sensor coordinates y_1 and y_2 are treated as uniformly distributed random variables in the range $(-U, U)$. Hence, the probability density function of y_2 is determined by Eq. (9), whereas the corresponding density function of random variable y_1 is given by

$$f_{y_1}(y_1) = \frac{1}{2U}[H(y_1 + U) - H(y_1 - U)]. \quad (41)$$

The two random variables are statistically independent. Hence, their joint probability density function is

$$f_{y_1 y_2}(y_1, y_2) = f_{y_1}(y_1)f_{y_2}(y_2)$$
$$= \frac{1}{4U^2}[H(y_1 + U) - H(y_1 - U)][H(y_2 + U)$$
$$- H(y_2 - U)]. \quad (42)$$

For the examined set of scanning lines, we have $\rho \geq 0$ and $\theta \in (-\frac{3\pi}{4}, -\frac{\pi}{4}) \cup (\frac{\pi}{4}, \frac{3\pi}{4})$. The following cases have to be distinguished.

- When $\theta \in (-\frac{3\pi}{4}, -\frac{\pi}{4})$, it follows from Eqs. (39) and (40) that

$$\theta = \text{arccot}\frac{y_2 - y_1}{2U} - \pi, \quad (43)$$

$$\rho = U\cos\left(\text{arccot}\frac{y_2 - y_1}{2U} - \pi\right) + y_1\sin\left(\text{arccot}\frac{y_2 - y_1}{2U} - \pi\right). \quad (44)$$

In this paper, we restrict the inverse function arccot to take only its principal values, i.e., values in the range $(0, \pi)$.

- When $\theta \in (\frac{\pi}{4}, \frac{3\pi}{4})$, we obtain from Eqs. (39) and (40):

$$\theta = \text{arccot}\frac{y_2 - y_1}{2U}, \quad (45)$$

$$\rho = U\cos\left(\text{arccot}\frac{y_2 - y_1}{2U}\right) + y_1\sin\left(\text{arccot}\frac{y_2 - y_1}{2U}\right). \quad (46)$$

The two 2×2 systems of Eqs. (43)–(46) have both a single solution in the corresponding intervals of variable θ. This solution is given by the same formula for both systems:

$$(y_{1_a}, y_{2_a}) = \left(\frac{\rho}{\sin\theta} - U\cot\theta, \frac{\rho}{\sin\theta} + U\cot\theta\right), \quad (47)$$

and is obtained by solving Eqs. (39) and (40) with respect to y_1 and y_2, and, also, by taking into account that, for the examined set of scanning lines, $\sin\theta \neq 0$. As a result of this and the theorem expressed by Eqs. (13)–(16), the formula that determines the joint probability density function $f^6_{\rho\theta}(\rho, \theta)$ is common for all intervals of variable θ. Considering Eq. (47), the application of the theorem expressed by Eqs. (13)–(16),
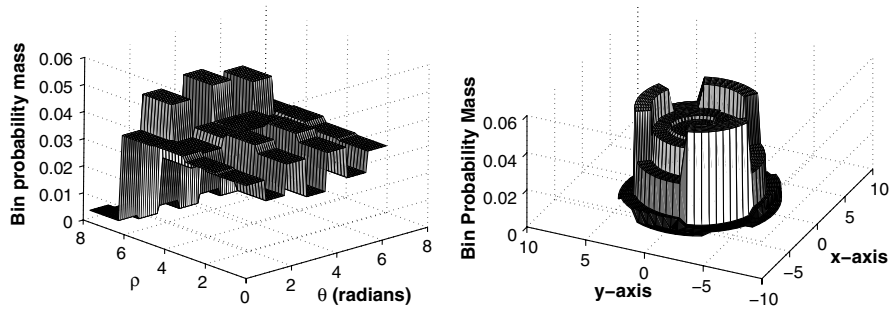
Fig. 9.   Left, map of probability mass for the binning of the numerical example; right, same map expressed in x–y coordinates.

for random variables y_1 and y_2 and the two systems of Eqs. (43)–(46), yields

$$J(y_{1_a}, y_{2_a}) = \begin{vmatrix} \frac{\partial \rho}{\partial y_{1_a}} & \frac{\partial \rho}{\partial y_{2_a}} \\ \frac{\partial \theta}{\partial y_{1_a}} & \frac{\partial \theta}{\partial y_{2_a}} \end{vmatrix} = \begin{vmatrix} \frac{\partial y_{1_a}}{\partial \rho} & \frac{\partial y_{1_a}}{\partial \theta} \\ \frac{\partial y_{2_a}}{\partial \rho} & \frac{\partial y_{2_a}}{\partial \theta} \end{vmatrix}^{-1} = -\frac{\sin^3 \theta}{2U}. \quad (48)$$

Taking into account Eqs. (47) and (48), we conclude from the theorem that

$$f^6_{\rho\theta}(\rho, \theta) = \left| \frac{2U}{\sin^3 \theta} \right| f_{y_1 y_2} \left(\frac{\rho}{\sin \theta} - U \cot \theta, \frac{\rho}{\sin \theta} + U \cot \theta \right). \quad (49)$$

Finally, by substituting Eq. (42) into Eq. (49), we obtain the joint density of ρ and θ for this set of scanning lines:
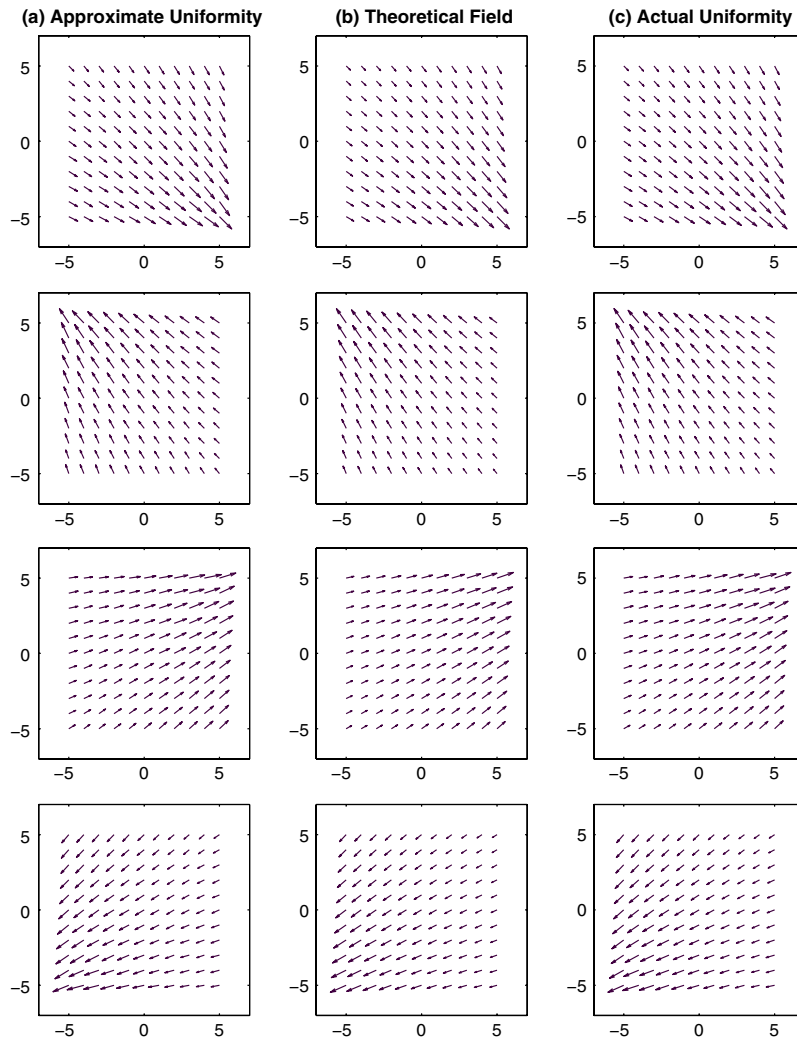

Fig. 10.   Simulation results when the location of the source of the electric field was (from top to bottom) at $(19, -19)$, $(-16, 21)$, $(24, 11.5)$, and $(-21, -12)$): (a) estimated vector field when estimation was based on weighted linear equations that approximate uniform sampling of the Radon space; (b) theoretical electric field as computed from Coulomb's law; (c) estimated vector field when the estimation was based on linear equations that correspond to actual uniform sampling of the Radon space.

$$f_{\rho\theta}^6(\rho,\theta) = \frac{\left|\frac{2U}{\sin^3\theta}\right|}{4U^2}\left[H\left(\frac{\rho}{\sin\theta} - U\cot\theta + U\right)\right.$$
$$- H\left(\frac{\rho}{\sin\theta} - U\cot\theta - U\right)\right]$$
$$\times \left[H\left(\frac{\rho}{\sin\theta} + U\cot\theta + U\right)\right.$$
$$\left. - H\left(\frac{\rho}{\sin\theta} + U\cot\theta - U\right)\right]. \qquad (50)$$

Next, we show how to determine the overall probability density function $f_{\rho\theta}(\rho,\theta)$ that the employed sensor arrangement of Fig. 1 generates in the Radon space by making use of the six individual densities. We considered six cases of scanning lines because the number of combinations of two boundary edges (where the two sensors are located) from a set of four boundary edges is $\frac{4!}{2!(4-2)!} = 6$. A basic assumption of our analysis was that a sensor lies on each of the four boundary edges of the square region with equal probability,

namely 1/4. In addition, we assumed that the two placements of the sensors are independent. Based on these two fundamental assumptions, it is obtained that each of the six cases of scanning lines has the same probability. This probability is equal to $2 \times \frac{1}{4} \times \frac{1}{3} = \frac{1}{6}$, where factor 1/3 gives the probability of the placement of the second sensor on a random boundary edge, having already placed the first sensor on a different edge. In addition, factor 2 is employed to account for the case of reverse placement of sensors to the same boundary edges. Also, we use multiplication due to the independence of the events. Considering the above and also taking into account the fact that the six cases, over which we partitioned the problem, are mutually exclusive and exhaustive, the application of the law of total probability for densities (see [30])

$$f_{\rho\theta}(\rho,\theta) = \sum_{i=1}^{6} f_{\rho\theta}^i(\rho,\theta|i^{\text{th}}\text{case})\text{Prob}(i^{\text{th}}\text{case}) \qquad (51)$$

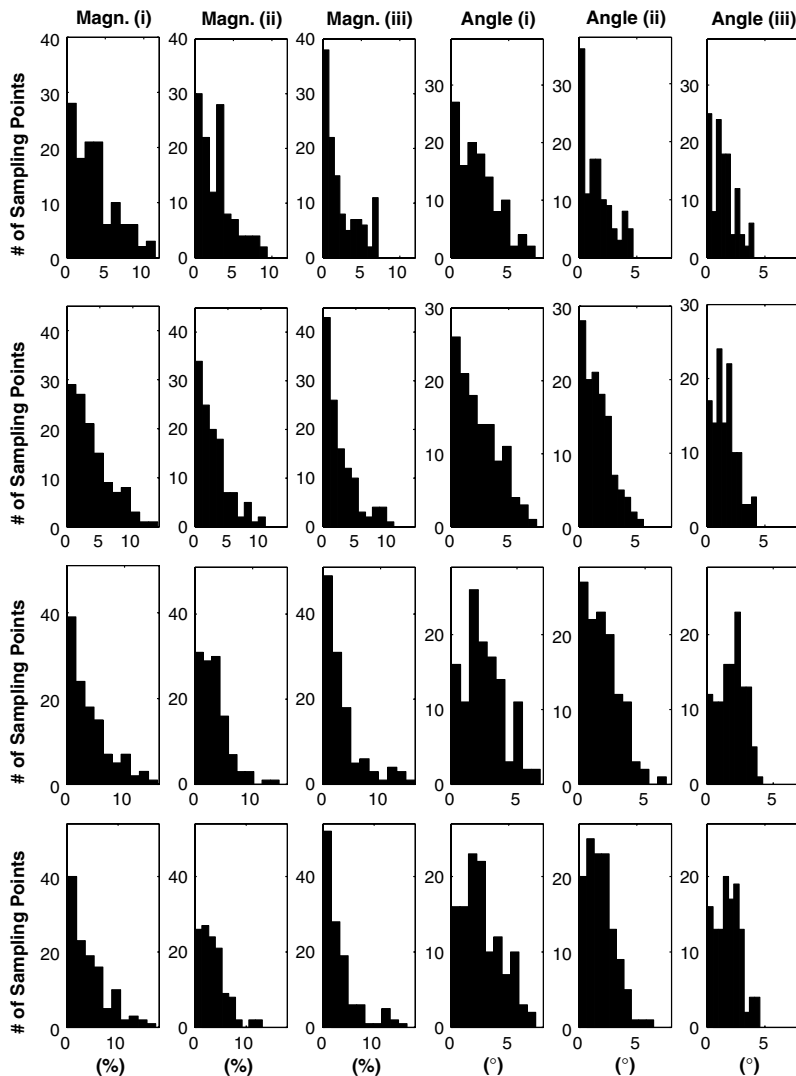yields, after substitution,

Fig. 11.   Left three columns, the relative errors in magnitude for case (i) uniform sensor placement along the boundary of the domain, as proposed in [28]; case (ii) same sensor arrangement as in (i), but also using weights to approximate uniform sampling in the (ρ,θ) space, as proposed in this paper; (iii) actual uniform sampling in the (ρ,θ) space. Right three columns, error in vector field orientation for the same cases. The location of the source of the electric field was (from top to bottom) at $(19,-19)$, $(-16,21)$, $(24,11.5)$, and $(-21,-12)$, respectively. We note that the histograms of the first and the fourth columns have heavier tails toward higher values.

$$f_{\rho\theta}(\rho,\theta) = \frac{1}{6}(f^1_{\rho\theta}(\rho,\theta) + f^2_{\rho\theta}(\rho,\theta) + f^3_{\rho\theta}(\rho,\theta) + f^4_{\rho\theta}(\rho,\theta)$$
$$+ f^5_{\rho\theta}(\rho,\theta) + f^6_{\rho\theta}(\rho,\theta)). \tag{52}$$

Figure 8 shows the regions of (ρ,θ) space that each of the six individual densities covers for $U = 5.5$. The same figure also shows the area that the overall probability density function $f_{\rho\theta}(\rho,\theta)$ covers in the (ρ,θ) space. It should be emphasized that the employed weights will not leave any region of the domain without data for the estimation, as all they do is try to imitate uniform sampling in the Radon space. However, near the corners of the domain, there may be very few lines covering the space, and therefore, their weights should be higher than lines through central regions. These high weights may amplify small errors in the measurements, and thus lead to less reliable estimations in the extremities of the domain.

Having obtained the probability density function of parameters (ρ,θ), $f_{\rho\theta}(\rho,\theta)$, generated by the sensor arrangement of Fig. 1, we next describe the method of calculating the weight by which each equation of system (4) should be multiplied. In order to obtain these weights, the (ρ,θ) space is divided into $R \times T$ nonoverlapping 2D bins of the same size, namely, R bins for the ρ parameter and T bins for the θ parameter. (The optimal choice of the number of bins used is discussed in [31].) Then, each of the $R \times T$ bins has a probability mass

$$p_b = \int_{\theta_{b_l}}^{\theta_{b_u}} \int_{\rho_{b_l}}^{\rho_{b_u}} f_{\rho\theta}(\rho,\theta)\mathrm{d}\rho\mathrm{d}\theta, \qquad b = 1,2,\ldots,RT, \tag{53}$$

where $(\theta_{b_l}, \theta_{b_u})$ and (ρ_{b_l}, ρ_{b_u}), with $\theta_{b_l} < \theta_{b_u}$ and $\rho_{b_l} < \rho_{b_u}$, determine the 2D region of definition of the bth bin. The mass in the entire (ρ,θ) plane (over the $R \times T$ bins) equals 1:

$$\int_{-\infty}^{+\infty} \int_{-\infty}^{+\infty} f_{\rho\theta}(\rho,\theta)\mathrm{d}\rho\mathrm{d}\theta = 1. \tag{54}$$

Hence, for any scanning line defined by parameter values (ρ_i, θ_i) that lies in the bth bin with probability mass p_b, the corresponding weight is

$$w_i = \frac{1}{p_b}\frac{1}{RT}, \qquad i = 1,2,\ldots,L, \tag{55}$$

where $\frac{1}{RT}$ is the probability mass of the bth bin, if the density were flat and L is the total number of the system's linear equations. The reasoning behind using these weights is to make the histogram of the Radon domain variables approximately flat.

After multiplying all equations (for all scanning lines) with the corresponding weights, the overdetermined system of equations is solved to obtain the reconstruction result. It must be noted that the linear equations are obviously not affected by the multiplication described above, since $\mathbf{Ax} = \mathbf{B}$ is equivalent to $\mathbf{WAx} = \mathbf{WB}$, where diagonal matrix $\mathbf{W}$ contains the weights along its diagonal. However, since the system is solved in a least-square error sense, this weight matrix does
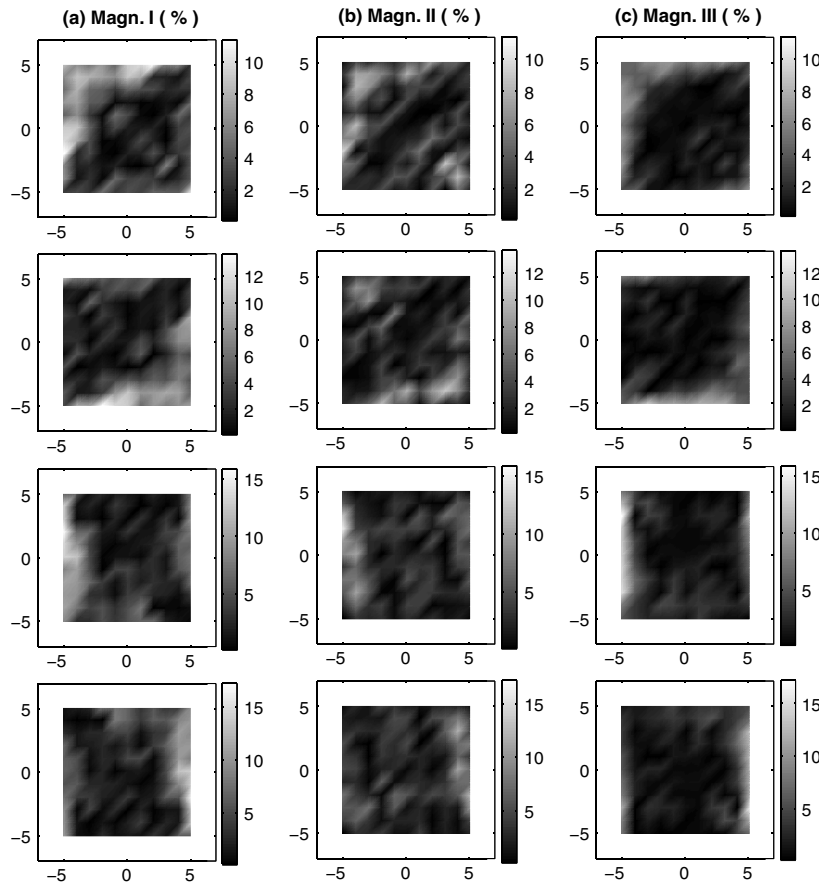

Fig. 12.   Maps of relative magnitude error for the corresponding cases in Fig. 10.
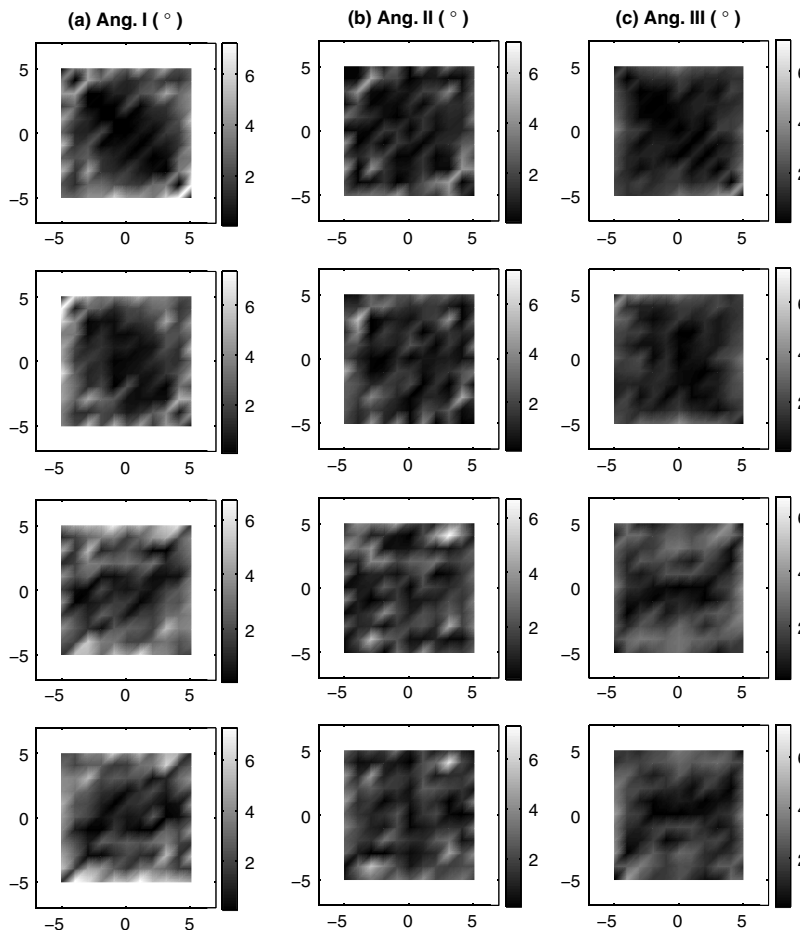
Fig. 13.   Maps of absolute error in orientation in degrees for the corresponding cases in Fig. 10.

affect the final solution. In Section 4, we present an example of static electric field estimation with the purpose of demonstrating the improvement in estimation quality by employing the probabilistic weights that compensate for the nonuniform sampling in the Radon domain, as proposed in this paper, over the case of [28], where the measurements were not weighed.

4. EXAMPLE: ELECTRIC FIELD IMAGING

We considered the case where the vector field under investigation was the electric field created by a static charge, the same as in [28]. Four different cases for the location of the source of the electric field are reported. We assumed that the boundary sensors measured the potential, so that

Table 1.   Average Relative Magnitude Estimation Error (%) per Pixel (ME) and the Average Absolute Angular Estimation Error (in Degrees) per Pixel (AE) for the Three Methods[a]

Source Location	ME (Not Weighted)	ME (Weighted)	ME (Uniform Sampling)	AE (Not Weighted)	AE (Weighted)	AE (Uniform Sampling)
$(19, -19)$	3.6791	2.8006	2.3790	2.2882	1.5400	1.4206
$(-16, 21)$	3.8114	2.8273	2.5339	2.4093	1.6217	1.5426
$(24, 11.5)$	4.0363	3.3109	3.1747	2.5210	1.8122	1.8720
$(-21, -12)$	4.3803	3.5199	3.2126	2.7013	1.8702	1.8594

[a](i) When data were not weighed, (ii) estimation method employed weights to approximate uniform sampling in the Radon domain, and (iii) when actual uniform sampling in the (ρ, θ) Radon space was used. Four different source locations are reported.

Table 2.   Average Errors for the Estimations of Fig. 14, Presented as the Results in Table 1

Source Location	ME (Not Weighted)	ME (Weighted)	ME (Uniform Sampling)	AE (Not Weighted)	AE (Weighted)	AE (Uniform Sampling)
$(19, -19), (-16, 21)$	13.5257	12.3761	7.6367	10.6294	7.6784	6.8202
$(-11, -24.5), (19, 19)$	16.3800	12.4449	11.8986	10.6106	8.2943	7.2703
6 sources, first case	10.3640	6.7949	6.2494	6.0522	4.0168	3.6089
6 sources, second case	12.2965	8.8954	8.1776	8.1711	5.3788	4.9961

the difference in the measurements between any two such sensors gave the vectorial Radon transform of the electric field. The potential of the field is given by $V = 10\frac{10}{\|\mathbf{r}\|}$. The corresponding electric field is $\bar{\mathbf{E}} = \frac{10\bar{\mathbf{r}}}{\|\bar{r}\|^3}$. Electric fields created by static charges are irrotational. The collected measurements $V = \int_L \bar{\mathbf{E}} \cdot \bar{\mathbf{dl}}$ are longitudinal measurements, collected along each line of integration. The field has to be band limited, and, in order to ensure this, and because the formulas we use contain a singularity, we placed the source of the field outside the reconstruction domain.

We employed the digital square reconstruction domain of Fig. 1 and chose $2U = 11$ as the domain size and $P = 1$ as the pixel size. Hence, the domain was sampled with 121 points and the number of the unknowns (the E_x and E_y components of the field at each sampling point) was 242. Regarding the data acquisition geometry, the above selection of values for parameters U and P resulted in 11 sensors in every side of the boundary of the square domain. For the simulations we present here, the potential in all these sensors was obtained by using Coulomb's law. We considered all possible voltage differences between pairs of these sensors, apart from sensors lying on the same border line. For the electric field estimation we relied only on these line-integral data.

We first formed the system of linear equations according to the analysis presented in [28] and reviewed in Section 2. The scanning line segments joining sensors were sampled with a step equal to 1 ($\Delta s = 1$). The number of linear equations was 726, whereas the number of the unknowns was 242. Hence, we obtained an overdetermined system of linear equations. Subsequently, these equations were weighed, according to the methodology proposed in Section 3. For the weight computation, we used $R = 5$ bins for the radial parameter and $T = 7$ bins for the angular parameter. These values were selected so that the bins were not too many for the number of available points to populate them with, and they were not too few to have inadequate resolutions. Other values of the same order of magnitude will not change the results (see also [31]). Then, in order to obtain the estimation results, we had to solve the overdetermined system of weighted linear equations.

Figure 9 shows the maps of the probability mass for the sinogram binning of this numerical simulation. We note that,
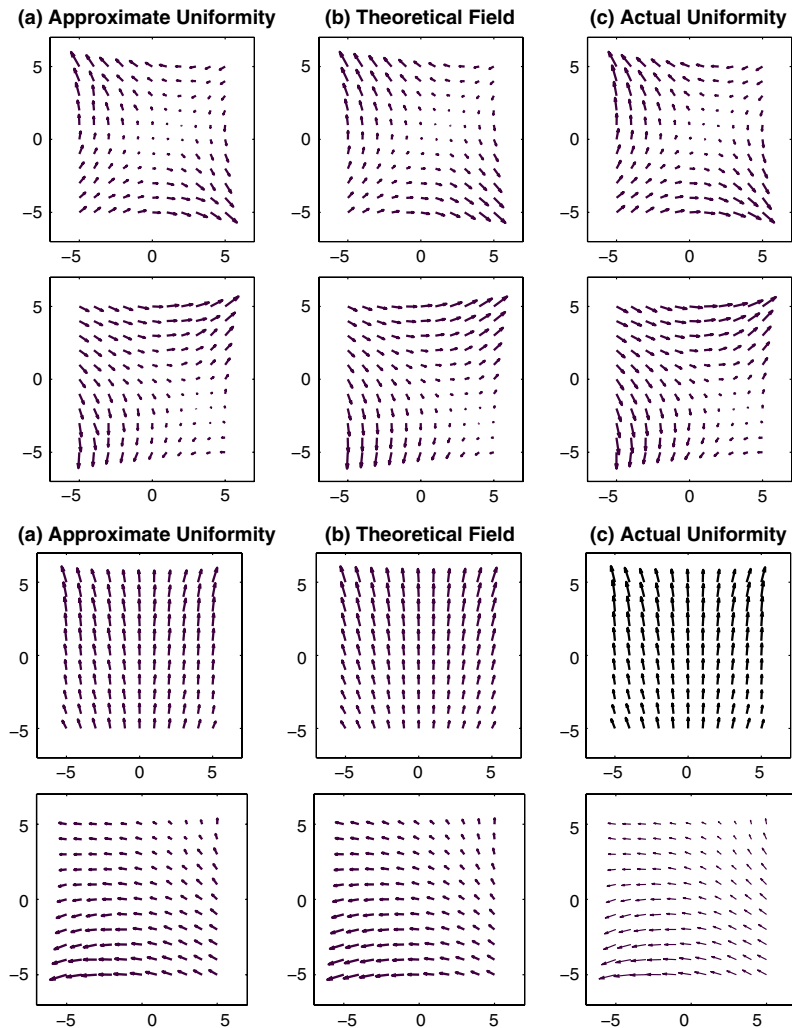

Fig. 14.   Simulation results for more complicated vector fields. Two top rows, fields created by two static sources, placed at $(19, -19)$ and $(-16, 21)$ (top) and $(-11, -24.5)$ and $(19, 19)$ (bottom). Bottom two rows, six sources placed at $(19, -19)$, $(-16, 21)$, $(24, 11.5)$, $(-21, -12)$, $(19, 19)$, and $(-11, -24.5)$. Third row, strengths of the sources are 4.1027 8.9365 0.5789 3.5287 8.1317 0.0986 (first case). Fourth row, strengths of the sources are 0.1530 7.4680 4.4510 9.3180 4.6600 4.1860 (second case). (a) Results with the proposed correction. (b) Theoretically computed result. (c) Results with uniform sampling of the Radon space.

as expected, larger weights appear in the corners of the domain (large ρ values), that are sparsely populated with lines.

A. Stability Considerations

Inverse problems, like the one described by the weighted system of linear equations we obtained above, suffer from the notorious ill-posed nature, in the sense of Hadamard [32]. As a result, the solution to these reconstruction problems endures stability deficiencies that are related to the solution's existence, uniqueness, and continuous dependency on the projection data.

A good measure of the degree of ill-posedness of a system of equations is the condition number, i.e., the ratio of the maximal to minimal eigenvalue of the matrix of coefficients. This measure gives us all the information we require about the ill-posedness, because the larger the value of the condition number, the more pronounced the ill-posedness of the inverse problem. For the simulations we carried out in this paper, the range of values of the condition number showed that the ill-posedness was noticeable but manageable and not serious. We obtained the least-squares error solution by applying the Gauss–Newton least-squares method [33], the most efficient numerical technique to perform least-squares estimations. The fact that the Gauss–Newton least-squares method might also return negative solutions is not a problem for vector field tomography as it is for conventional scalar tomography. Further, the sizes of the associated system matrices were not prohibitively large to prevent us from using the Gauss–Newton least-squares method. Moreover, it must be noted that, since the residual we computed by using the least-squares Gauss–Newton method was not large when compared with the solution vector, there was no need to use the Cholesky method [34]. We also tested the Householder orthogonalization method [35], which is a numerically useful
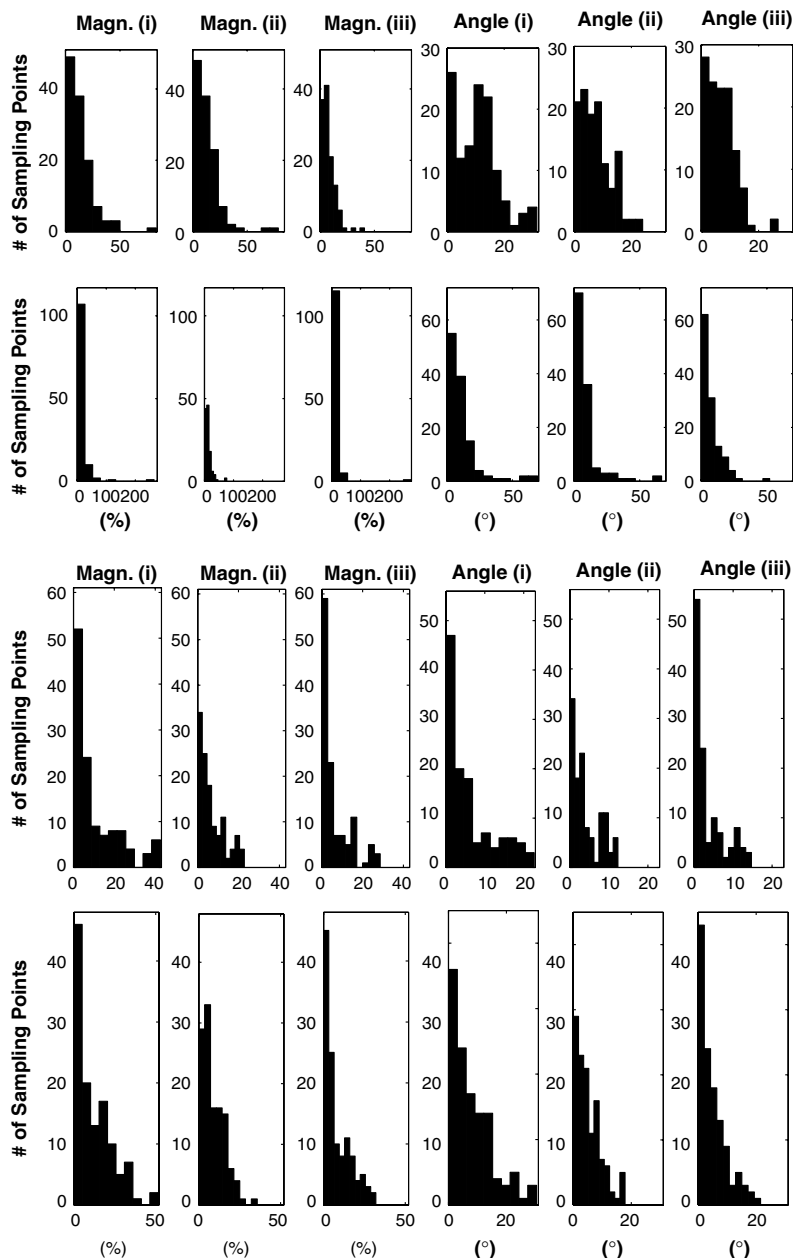

Fig. 15.   Histograms of errors for the estimations of Fig. 14, arranged as in Fig. 11.
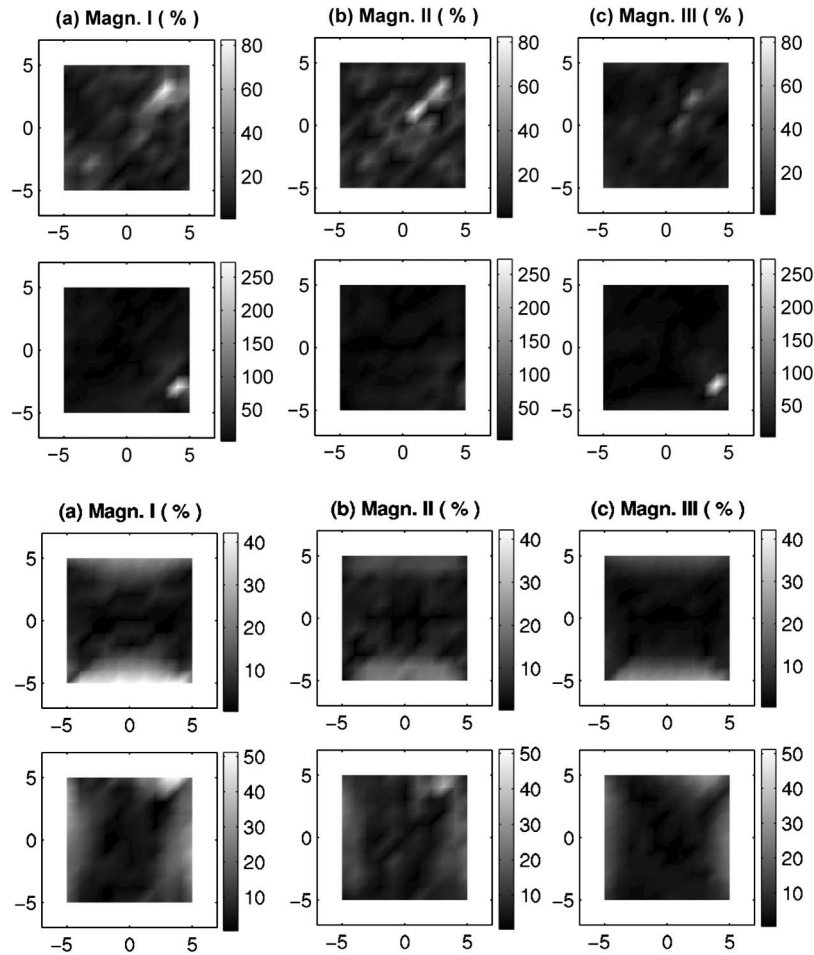
Fig. 16.   Maps of relative magnitude error for the estimations of Fig. 14, arranged as in Fig. 12.

procedure in order to solve least-squares value problems for cases where the condition number of the matrix of coefficients is large [36]. However, the results we obtained were identical with the results we obtained using the Gauss–Newton least-squares method.

B. Field Estimation

The estimation results, namely the solution of the overdetermined systems of the weighted linear equations, are shown in Fig. 10(a) for four different source locations. For the sake of comparison, Fig. 10(b) depicts the respective theoretical electric fields that were obtained by using directly the governing Coulomb's law, while Fig. 10(c) shows the corresponding estimated fields when we applied direct uniform sampling in the Radon domain parameters, using the sampling steps recommended in [37,38], namely $\Delta\theta = 2°$ and $\Delta\rho = 0.5$. By careful inspection of Fig. 10, we may say that the directions of the vectors that were estimated, based on the boundary voltages, are almost identical to the directions of the vectors that were obtained by using Coulomb's law, since, in all three cases, the vectors are oriented toward the source of the field. Furthermore, vectors in all three fields reduce in magnitude with the distance from the source, as expected, even though the estimated vectors seem to reduce a bit more slowly than those computed by the application of Coulomb's law.

In order to demonstrate the improvement in estimation accuracy gained by using probabilistic weights over the case of [28], where the measurements were not weighed, we present in Fig. 11 the histograms of the errors for these two cases. Figure 11 also shows the respective histograms of the errors that were obtained when actual uniform sampling of the projection space was used. To achieve such sampling we had either to use about 3960 sensors, instead of 44, or increase the total scanning time 180 times by employing a rotating geometry. Figures 12 and 13 are the error maps for the same cases, for the magnitude and orientation of the estimated field.

We can see in Fig. 11 that, as expected, the employment of actual uniform sampling in the (ρ, θ) space resulted in more accurate estimation than the use of probabilistic weights and uniform sensor placement. However, to achieve the accuracy of uniform sampling in the (ρ, θ) space, we either have to overcome sensor placement impracticalities or use a rotating acquisition system at the expense of temporal efficiency.

To obtain a quantitative idea of the observations made in Fig. 11, in Table 1, we tabulate the average values per sampling point of the relative magnitude and absolute angular estimation errors for the original estimation method [28], the modified weighted estimation technique proposed in this paper, and the estimation method that employs actual uniform sampling of the projection space.
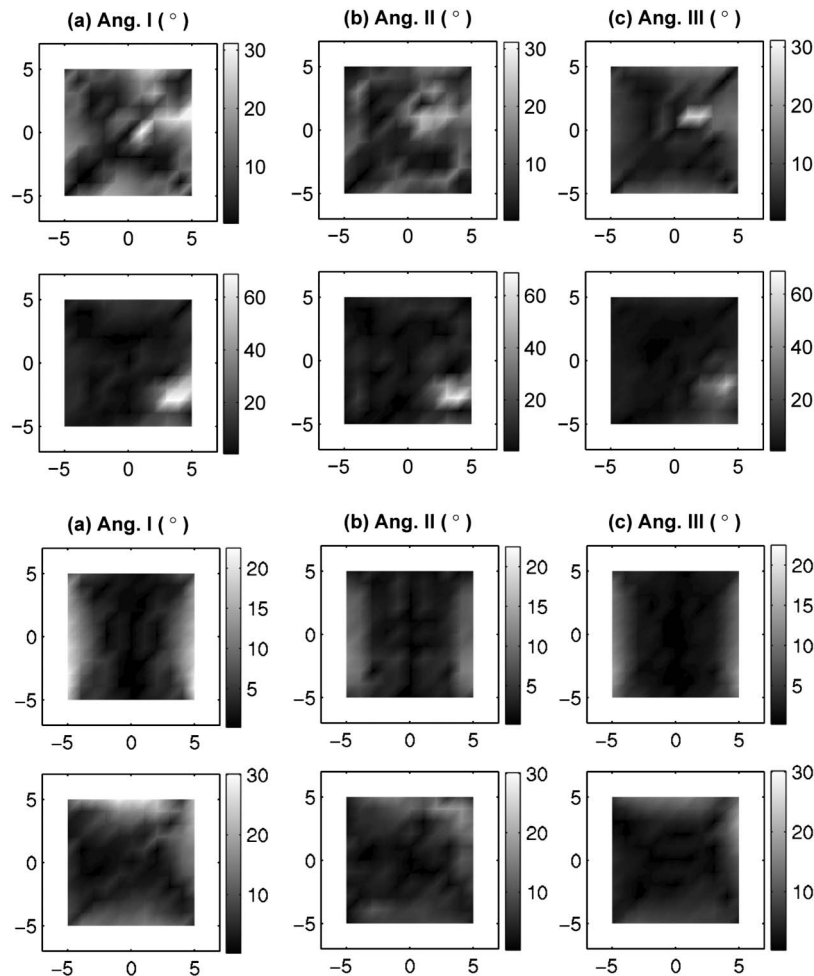
Fig. 17.   Maps of absolute error in orientation, measured in degrees, for the estimations of Fig. 14, arranged as in Fig. 13.

Figures 14–17 show the results of estimation of some fields that are created by two- and six-point sources of various strengths. The corresponding quantitative results are given in Table 2.

By inspecting Tables 1 and 2, we observe the effectiveness of the probabilistic weights, proposed in this paper, in suppressing the estimation error. In particular, we found that we had only 7% increase in the estimation error when the probabilistic weights were used as opposed to 46% when they were not used, while keeping the number of required sensors or the total scanning time to orders of magnitude lower than the case of actual uniform sampling in the (ρ, θ) space. For example, using only M sensors, we can consider approximately $M!$ scanning lines. If we want to retain the same number of scanning lines and have uniform sampling in the (ρ, θ) space, we would need either about $2M!$ sensors to be placed at very specific locations along the boundary of the estimation domain, or a 180-fold increase in the total scanning time by employing a rotating scanning configuration.

5. DISCUSSION AND CONCLUSIONS

It is well recognized that vector field tomography has substantial potential for many applications. The analysis of the 2D vector field reconstruction problem in the continuous domain and the employment of a Fourier slice theorem-based approach has led to an underdetermined problem [5,11,12]. However, it has been demonstrated in [28] that, in the discrete domain and under the assumption of a band-limited vector field, which means that singularities are excluded from the reconstruction domain, it is possible to estimate both components of the 2D vector field at the sampling points of the digitized bounded reconstruction domain based only on a finite number of line-integral data.

According to the theory of the Radon transform [29], a necessary requirement to produce reconstruction results with the accuracy desired in medical imaging is to sample uniformly the (ρ, θ) Radon space. However, the technique that was proposed in [28] assumed that the measurements were collected by sensors that followed uniform distribution along the boundary of the reconstruction domain. Such a sensor placement might be the most practical, however, it does not result in scanning lines that follow uniform distribution in the (ρ, θ) projection space. On the other hand, sampling the Radon parameter domain uniformly imposes serious constraints on space or time.

In this paper, we compensated for the lack of uniformity in the (ρ, θ) projection space by employing probabilistic weights. The equations created by placing the sensors uniformly along the domain boundary were multiplied with weights designed to transform the distribution of the sampled (ρ, θ) parameters

into a uniform one. Simulation results indicated that this resulted in a significant reduction of both the angular and magnitude estimation error, as compared with the case where unweighted data from sensors were used, and an insignificant difference with the estimations obtained when the (ρ, θ) space was sampled uniformly with either 90 times more sensors or a 180-fold increase in the total scanning time. Further, the condition number of the system matrices we solve was computed for all cases both before and after using weights. It was found that the employment of the proposed probabilistic weights decreases significantly the condition number in each case; hence, the system becomes less ill-conditioned.

The proposed method decreases the estimation error without increasing either the number of sensors or the processing time, while maintaining a practical sensor placement configuration. The reason that the overall processing time does not increase is that the calculation of the weights is based on the known and predetermined sensor configuration. Hence, this calculation can be performed in advance (offline).

REFERENCES

1. S. P. Juhlin, "Doppler tomography," in *Proceedings of the 15th Annual International Conference of the IEEE Engineering in Medicine and Biology Society* (EMBC, 1993), pp. 212–213.
2. Y. K. Tao, A. M. Davis, and J. A. Izatt, "Single-pass volumetric bidirectional blood flow imaging spectral domain optical coherence tomography using a modified Hilbert transform," Opt. Express **16**, 12350–12361 (2008).
3. N. P. Efremov, N. P. Poluektov, and V. N. Kharchenko, "Tomography of ion and atom velocities in plasmas," J. Quant. Spectrosc. Radiat. Transfer **53**, 723–728 (1995).
4. B. M. Howe, P. F. Worcester, and R. C. Spindel, "Ocean acoustic tomography: mesoscale velocity," J. Geophys. Res. **92**, 3785–3806 (1987).
5. W. Munk and C. Wunsch, "Observing the ocean in the 1990s," Phil. Trans. R. Soc. A **307**, 439–464 (1982).
6. D. Rouseff, K. B. Winters, and T. E. Ewart, "Reconstruction of oceanic microstructure by tomography: a numerical feasibility study," J. Geophys. Res. **96**, 8823–8833 (1991).
7. S. A. Johnson, J. F. Greenleaf, M. Tanaka, and G. Flandro, "Reconstructing three-dimensional temperature and fluid velocity vector fields from acoustic transmission measurements," ISA Trans. **16**, 3–15 (1977).
8. D. M. Kramer and P. C. Lauterbur, "On the problem of reconstructing images of non-scalar parameters from projections. Applications to vector fields," IEEE Trans. Nucl. Sci. **26**, 2674–2677 (1979).
9. S. J. Norton and M. Linzer, "Correcting for ray refraction in velocity and attenuation tomography: a perturbation approach," Ultrason. Imag. **4**, 201–233 (1982).
10. S. J. Norton, "Tomographic reconstruction of 2-D vector fields: application to flow imaging," Geophys. J. Int. **97**, 161–168 (1989).
11. S. J. Norton, "Unique tomographic reconstruction of vector fields using boundary data," IEEE Trans. Image Process. **1**, 406–412 (1992).
12. H. Braun and A. Hauck, "Tomographic reconstruction of vector fields," IEEE Trans. Signal Process. **39**, 464–471 (1991).
13. K. B. Winters and D. Rouseff, "A filtered backprojection method for the tomographic reconstruction of fluid vorticity," Inverse Probl. **6**, L33–L38 (1990).
14. K. B. Winters and D. Rouseff, "Tomographic reconstruction of stratified fluid flow," IEEE Trans. Ultrason. Ferroelectr. Freq. Control **40**, 26–33 (1993).
15. H. K. Aben, "Kerr effect tomography for general axisymmetric field," Appl. Opt. **26**, 2921–2924 (1987).
16. G. W. Faris and R. L. Byer, "Three-dimensional beam-deflection optical tomography of a supersonic jet," Appl. Opt. **27**, 5202–5212 (1988).
17. H. M. Hertz, "Kerr effect tomography for nonintrusive spatially resolved measurements of asymmetric electric field distributions," Appl. Opt. **25**, 914–921 (1986).
18. M. Zahn, "Transform relationship between Kerr-effect optical phase shift and non-uniform electric field distributions," IEEE Trans. Dielectr. Electr. Insul. **1**, 235–246 (1994).
19. V. A. Sharafutdinov, "Tomographic problem of photoelasticity," Proc. SPIE **1843**, 234–243 (1992).
20. H. Aben and A. Puro, "Photoelastic tomography for three-dimensional flow birefringence studies," Inverse Probl. **13**, 215–221 (1997).
21. S. E. Segre, "The measurement of poloidal magnetic field in a tokamak by the change of polarization of an electromagnetic wave," Plasma Phys. **20**, 295–307 (1978).
22. A. Schwarz, "Three-dimensional reconstruction of temperature and velocity fields in a furnace," Part. Part. Syst. Charact. **12**, 75–80 (1995).
23. P. Juhlin, "Principles of Doppler tomography," LUTFD2/(TFMA-92)/7002+17P, Lund Institute of Technology, Sweden, 1992.
24. L. Desbat and A. Wernsdorfer, "Direct algebraic reconstruction and optimal sampling in vector field tomography," IEEE Trans. Signal Process. **43**, 1798–1808 (1995).
25. T. Sato, H. Aoki, and O. Ikeda, "Introduction of mass conservation law to improve the tomographic estimation of flow-velocity distribution from differential time-of-flight data," J. Acoust. Soc. Am. **77**, 2104–2106 (1985).
26. I. Jovanovic, L. Sbaiz, and M. Vetterli, "Acoustic tomography for scalar and vector fields: theory and application to temperature and wind estimation," J. Atmos. Ocean. Technol. **26**, 1475–1492 (2009).
27. D. Rouseff and K. B. Winters, "Two-dimensional vector flow inversion by diffraction tomography," Inverse Probl. **10**, 687–697 (1994).
28. M. Petrou and A. Giannakidis, "Complete tomographic reconstruction of 2-D vector fields using discrete integral data," Comp. J. (to be published).
29. S. R. Deans, *The Radon Transform and Some of Its Applications* (Wiley, 1983).
30. A. Papoulis, *Probability, Random Variables, and Stochastic Processes*, 2nd ed. (McGraw-Hill, 1984).
31. A. Giannakidis and M. Petrou, "Sampling bounds for 2D vector field tomography," J. Math. Imaging Vision **37**, 151–165 (2010).
32. J. Hadamard, "Sur les problèmes aux dérivées partielles et leur signification physique," Princeton University Bulletin **13**, 49–52 (1902).
33. C. F. Gauss, *Theoria Motus Corporum Coelestium* (Perthes, 1809).
34. I. N. Bronshtein, K. A. Semendyayev, G. Musiol, and H. Muehlig, *Handbook of Mathematics* (Springer, 2003).
35. H. R. Schwarz, *Numerische Mathematik* (B. G. Teubner, 1986).
36. H. Schwetlick and H. Kretzschmar, *Numerische Verfahren für Naturwissenschaftler und Ingenieure* (Fachbuchverlag, 1991).
37. M. Petrou and A. Kadyrov, "Affine invariant features from the trace transform," IEEE Trans. Pattern Anal. Machine Intell. **26**, 30–44 (2004).
38. A. Kadyrov and M. Petrou, "Affine parameter estimation from the trace transform," IEEE Trans. Pattern Anal. Machine Intell. **28**, 1631–1645 (2006).